MULTIPHASE FLUID HAMMER WITH CRYOGENIC FLUIDS

J.-B. Gouriet [(1)], A. Huertas-Martinez[(1)], J.-M. Buchlin [(1)], M.-R. Vetrano [(1)] and J. Steelant [(2)]

[(1)] von Karman Insitute for Fluid Dynamics, Chaussée de Waterloo 72, 1640 Rhode-St-Genèse (Belgium), gouriet@vki.ac.be, buchlin@vki.ac.be, vetrano@vki.ac.be
[(2)] ESA-ESTEC, Keplerlaan 1, 2200 AG Noordwijk (The Netherlands), johan.steelant@esa.int

KEYWORDS: water hammer, propellant lines, cryogenic flows, two-phase flows, EcosimPro, ESPSS library

ABSTRACT:

The von Karman Institute with the support of the European Space Agency is studying since several years multiphase fluid hammer phenomena occurring during priming processes in propulsion systems. After having built and analyzed an experimental database on multiphase fluid hammer with liquids at room temperature such as water, ethanol and acetaldehyde (representative for storable propellants), a new test facility has been developed to extend the database to liquid nitrogen (representing cryogenic propellants). The fluid hammer is characterized experimentally though time-resolved pressure and temperature measurements at the impact location. An experimental feasibility study based on two different test conditions (i.e. two different back pressures in the line) has been done on this new facility. In parallel to this experimental work, a numerical investigation has been carried out with the 1D numerical code EcosimPro/ESPSS. The cryogenic fluid hammer facility has been modeled and the two test conditions have been simulated to evaluate the capability of the 1D code to reproduce the fluid hammer and the resulting multiphase phenomena.

1. INTRODUCTION

Spacecraft or upper stages operating in low-pressure or vacuum conditions induce complex multiphase phenomena in the propulsion system [1]. The present study focuses on one of these phenomena which takes place during the priming operation and known as water hammer. This operation starts with the opening of a fast opening valve and results in the filling and pressurization of the propellant lines. The liquid flow finds all the downstream valves closed, and it is precisely at the dead ends of the piping system that the water hammer pressure fronts are generated.

This operation may turn out to be critical if the corresponding overpressures are not correctly taken into consideration in the pipe line and in the sub-system dimensioning (flow control valve, sensors, filters…). Furthermore, the propellant line can be vacuum pumped or filled with a non-condensable gas (NCG) at low pressure, which complicates the classical water hammer due to various multi-phase phenomena such as cavitation, flashing and boiling front. The pressure seen by the liquid front can be below the liquid vapor pressure, resulting in a cavitation regime where the liquid flow is transformed into two-phase flow, together with the absorption and desorption into the liquid propellant of NCG if initially present in the line. On top of that, the propellant is pressurized in the tanks by means of a pressuring gas, which can be absorbed into the liquid propellant during storage and be desorbed during the priming process. Finally, there is also the fluid-structure interaction due to the increase of the pipe cross section at the water hammer front location

The previous description of the water hammer phenomena is compatible with storable propellants such as Mono Methyl Hydrazine (MMH) or Nitrogen TetrOxide (NTO) [2]. The use of cryogenic fluids such as LO2 and LH2 as liquid propulsion is increasing furthermore the complexity of the multiphase flow phenomena. Indeed, a cryogenic liquid has its temperature usually below -150ºC, when introduced into a piping system having a normal operative temperature from -50ºC to +30ºC. The high temperature difference induces a high thermal flux from the solid to the liquid. This high thermal flux may result in an intense evaporation of

the liquid and a sudden variation of the solid temperature with the associated sharp variation of the thermal stress. This transient phenomenon occurs during the priming operation and is usually referred as the system chilldown. This phenomenon introduces complication through a violent thermal heat transfer that accentuates the ebullition and the two-phase character of the flow.

Today most of the numerical models of the fluid hammer phenomenon in fluid networks are established on the basis of results obtained with water in simple configurations. Due to the complexity of the multi-phase phenomena occurring in spacecrafts hardware during the priming process (fluid hammer, cavitation, flashing, boiling front, absorption, desorption, conjugate heat transfer) and the lack of literature describing experimental campaigns with all the specifications of the above configuration, the physical models implemented in the numerical codes cannot be validated properly. To that end, the creation of an extensive database is necessary for the improvements of the numerical tools [4,5,6,7].

The von Karman Institute with the support of the European Space Agency is studying since several years multiphase fluid hammer phenomena occurring during the priming process. In a preceding study [2,3,4], an extensive database with liquids at room temperature, such as water, ethanol and acetaldehyde, has been built by varying a large number of parameters (pipe configuration, initial vacuum condition in the pipe, liquid properties and saturation condition of the liquid) leading to important findings on the fluid hammer phenomena. In parallel, experiments have been performed with real propellants MMH and NTO at ONERA [10] on a certified facility which re-uses parts of the facility used in [4] for comparison purposes. The first objective of the present study is to extend the existing fluid hammer database to low temperature liquids such as liquid nitrogen (LN2) to address the additional complexity due to their specific thermodynamic characteristics. The second objective is to pursue the benchmarking of the 1D numerical code EcosimPro/ESPSS with the new data collected.

First, the paper focuses on the description of the new cryogenic facility and on the experimental feasibility study and then, on the confrontation with the numerical predictions.

2. MULTIPHASE FLUID HAMMER EXPERIMENTS

2.1. Cryogenic experimental facility

A dedicated cryogenic facility representative to a priming process in propellant lines has been designed and assembled to extend the existing fluid hammer database towards cryogenic fluids. This facility allows characterizing the discharge of pressurized Liquid Nitrogen (LN2) into a closed line initially vacuum pumped or filled at different pressure levels with Nitrogen Gas (GN2) or with NCG (GHe). Figure 1 shows a layout of this facility, which integrates the elements affecting the fluid hammer occurrence, i.e. the pressurized liquid reservoir, the fast opening valve (FOV) and the test line with a closed end.

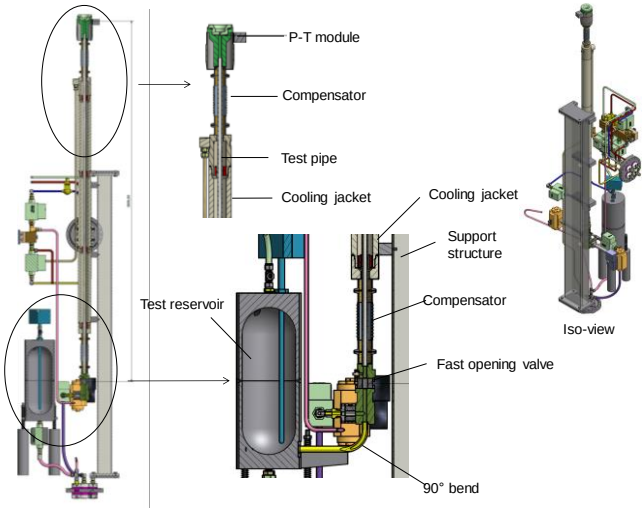

Figure 1. Facility layout for cryogenic fluids

The test line is a stainless steel straight pipe of 2 meters long oriented vertically (diameter 5/8", thickness 0.125"). The liquid front flows in this pipe from the bottom to the top. The 6-liters pressurized reservoir is connected to the bottom part of the test line through a 90° bend with a large radius of curvature in order to minimize the pressure losses. The fast opening valve (FOV) is a high-pressure cryogenic ball valve (model 60C, Triad process) driven with a pneumatic actuator (model AD-005, Radius). The diameter of the ball orifice (9.65mm) corresponds to the inner diameter of the test pipe. Its opening time has been measured before and after chilldown by high-speed imaging. The flow passage area varies from 0% to 100% in approximatively 100ms as shown in Figure 2. This opening time should stay below the traveling time of the liquid front till the end of the line to have minimal effect on the pressure surge [0,9]. This assumption has been confirmed during the experiments; the liquid front needs more than 200ms to reach the

closed end of the line.

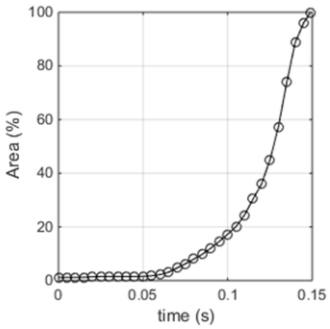

Figure 2. Opening area of the FOV versus time

In order to characterize only the multiphase fluid hammer phenomena caused by the abrupt stopping of the cryogenic flow in motion and not by the chilldown process, the complete test section shall be completely chilled down before opening the FOV. The test pipe is cooled down from its exterior side with a circulation of cryogenic liquids into an external jacket. The chilldown process is monitored with resistance temperature detectors (RTDs) (model Cernox CX-1050, Lake Shore Cryotronics Inc.) positioned at different locations of the test section.

Figure 3 shows that the complete test section and the cryogenic components operate in a vacuum chamber (Pvc < 100Pa) in order to limit heat transfer with the environment. This chamber is equipped with several ports to mount electrical and liquid/gas feedthroughs as well as optical windows. A vertical rectangular hollow section fixed inside the chamber supports the fluid hammer set-up.

Figure 3. Cryogenic facility inside the vacuum chamber

The cryogenic facility includes also service components such as a vacuum pump, a 600-liters pressurized LN2 dewar, pressurized NCG cylinders and solenoid valves to properly set-up the test conditions. The facility is also equipped with cryogenic check-valves and safety valves to protect the components and the lines against overpressure.

2.2. Measurement modules

The characterization of the wave front induced by the fluid hammer is achieved with interchangeable instrumented modules attached at the top of the line. Two types of modules, sketched in Figure 4, are considered:
(1) a pressure measurement module, referred as P-module, with a single pressure transducer (model CTL-190M, Kulite semiconductor) flush-mounted on the closed end. The module has been manufactured in one piece and the transducer is aligned with the pipe centerline.
(2) a combined pressure-temperature measurement module, referred as P-T module, with a pressure transducer (CTL-190M) and a temperature transducer (RTWH coaxial type-E thermocouple, model KL). Both sensors are slightly shifted outwards to fit together. The junction of the thermocouple is submerged in the fluid zone (protrusion ~1mm).

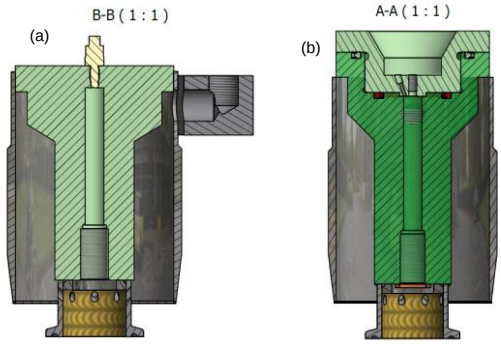

Figure 4. Instrumented modules: (a) P-module, (b) P-T module)

The coaxial thermocouple has been calibrated with its acquisition chain from 77K to 288K with a RTD sensor (model Cernox CX-1050, Lake Shore Cryotronics Inc.) chosen as reference. Both sensors measure the temperature of a calibration cell made in copper (left-hand picture in figure 5). Special attention has been paid to the design of this cell to neglect the temperature gradient between the installation ports of the two sensors. The cell initially at room temperature is cooled down by flowing LN2 in its internal cooling channel. The calibration starts when the cell stabilizes at 77K. The cooling is stopped and both signals from the reference sensor and from the thermocouple are recorded till the cell returns to room temperature. The right-hand graph plotted in Figure 5 shows that the reference temperature and the calibrated thermocouple signal overlaps well from 77K and 288K.

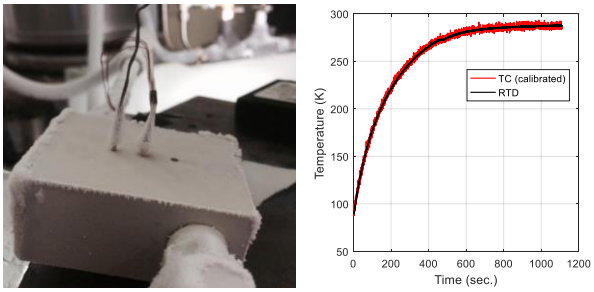

Figure 5. Calibration of the coaxial thermocouple

2.3. Testing procedure

The test procedure starts with purging cycles of the complete facility (vacuum pumping and flushing with GN2). Then, the test line is vacuum pumped or filled at a desired pressure with GN2. After the chilldown of the facility, the reservoir is partially filled with LN2 and pressurized at the test pressure with GN2. The 90º bend connecting the pressurized reservoir to the FOV is purged to remove the vapor that might be entrapped. The fluid hammer test starts by opening the FOV.

2.4. Pressure measurements (P-module)

Two tests have been performed with the P-module at the same initial conditions to check the measurement repeatability (table 1).

Parameters	Test #1	Test #2
Reservoir pressure [bar]	15.5+/-0,7	15.2+/-0,7
Line pressure [bar]	0.19+/-0,05	0.26+/-0,05
Reservoir temp. [K]	84+/-0,05	82+/-0,05
Module temp. [K] (RTD)	89+/-0,05	87+/-0,05

Table 1. Initial conditions for P-module experiments

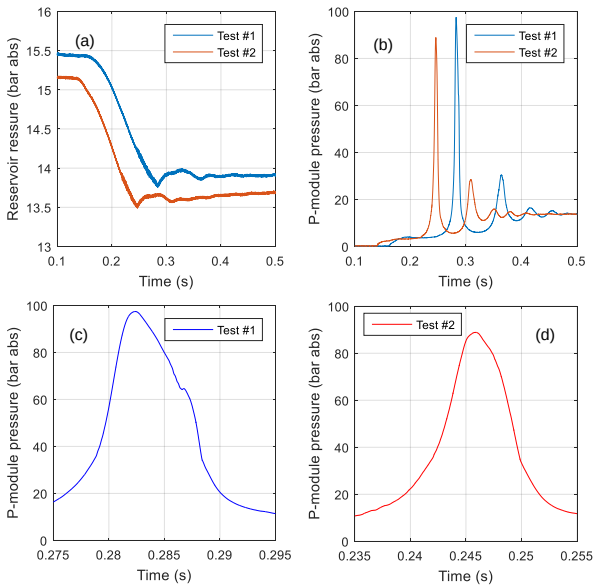

Figure 6. Pressure evolution in the reservoir (a) and at the closed end (b) (c) (d) (P-module experiments)

The time-resolved pressure is measured during the fluid hammer occurrence both in the pressurized reservoir and at the closed end of the line (Figure 6). The time t=0 corresponds to the exact moment when the electrical opening signal is sent to the FOV.

The pressure in the reservoir starts decreasing at t=155ms and t=138ms for test #1 and test #2, respectively, when the pressurized liquid leaves the reservoir (Figure 6 a). The origin of this delay between the two tests is not clearly identified today. It could come from a delay in the valve opening or from different flow conditions through the valve (flashing). The pressure in the reservoir continues to decrease till the compression wave generated at the impact location travels back and reaches the reservoir. Afterwards, low-amplitude fluctuations appear in the pressure signals due to the pressure waves travelling back and forward in the line.

The time-resolved pressure measurement at the closed end of the line is the data that better characterizes the fluid-hammer phenomenon (Figure 6 b-c-d). This pressure starts increasing when the pressurized liquid leaves the reservoir and passes through the FOV. Indeed, the liquid goes below its saturation pressure and vaporizes producing almost instantaneously large amount of vapor. This vaporization continues until the pressure in the line reaches the saturation pressure of LN2 (~2.7bar at 87K). At this moment, the liquid stops vaporizing and the pressure in the line remains constant until the liquid front reaches the proximities of the closed end and compresses the vapor phase creating the first pressure peak. The maximum pressure corresponds to the moment when the liquid front impacts the closed end. The generated compression wave travels downwards and comes back as an expansion wave after being reflected at the reservoir. The arrival of this expansion wave accelerates the liquid column downwards. Then, the liquid front comes back again to the closed end and induces the second pressure peak. From this point, this behavior is repeated several times till the phenomenon is completely damped.

Considering the sensitivity of the studied phenomena with the initial conditions, the measurement repeatability is considered as satisfactory. Indeed, the pressure signals from test #1 and test #2 follow the same temporal evolution both at the reservoir and at the end of the line. The main difference between the repetition tests comes from the time delay of ~17ms at the opening of the FOV. A dimensionless representation is also

proposed in Figure 7a to compare the pressure attenuation. In this representation, the maximum pressure level reached at each peak is normalized by the first pressure surge (P_1) and the time occurrence is divided by the delay between the first and the second peak ($\Delta t_1=t_2-t_1$). Both tests give the same attenuation pattern. For comparison, Figure 7b plots the results obtained by Lema et al. [3,4] with non-cryogenic liquids at saturated conditions, i.e. water, ethanol and acetaldehyde. It is worth mentioning that we have to pay attention by doing such comparison because the fluid hammer facility used by Lema et al. [3,4] is not exactly the same (ID 5.55mm instead of 9.53mm, pipe oriented downward instead of upward…). The initial pressure set in the reservoir (i.e. 20bar) and in the test line (i.e. 0.1bar) are also different. We can see from Figure 7 that the signal attenuation is significantly faster with liquid nitrogen than with water and ethanol. For acetaldehyde, the attenuation of the second pressure peak is very similar to the case with liquid nitrogen. However, the attenuation is faster with liquid nitrogen for the following peaks. This faster attenuation with liquid nitrogen than with the non-cryogenic liquids is very probably due to the large amount of vapor produced at a high rate during this time interval.

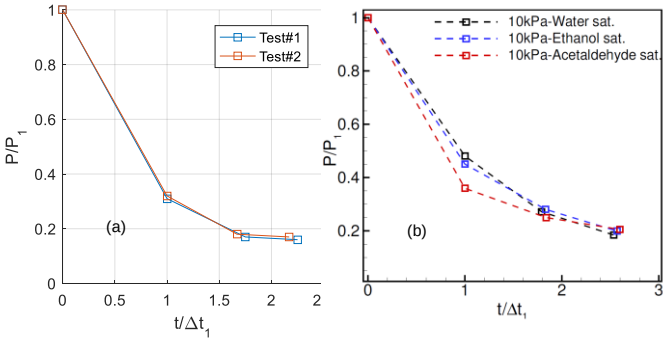

Figure 7. Dimensionless pressure signal attenuation for liquid nitrogen (a) and non-cryogenic liquids [3] (b)

2.5. Combined pressure and temperature measurements (P-T module)

Three tests have been performed with the P-T module at the same initial conditions to check the measurement repeatability, in particular of the fluid temperature measurement at the impact location (table 2). The main difference with the P-module experiments (table 1) is the higher initial pressure in the test line.

The time-resolved pressure and temperature are measured in a synchronous way at the closed end of the line during the fluid hammer occurrence. The results are plotted in Figure 8.

Parameters	Test #3	Test #4	Test #5
Reservoir pressure [bar]	14.1+/-0,7	13.7+/-0,7	14.3+/-0,7
Line Pressure [bar]	0.84+/-0,05	0.84+/-0,05	0.92+/-0,05
Reservoir temp. [K]	81.45+/-0,05	83.15+/-0,05	82.15+/-0,05
Module temp. [K] (RTD)	92.95+/-0,05	92.25+/-0,05	93.32+/-0,05
Module temp. [K] (TC)	92.45	92.26	93.65

Table 2. Initial conditions for P-T module experiments

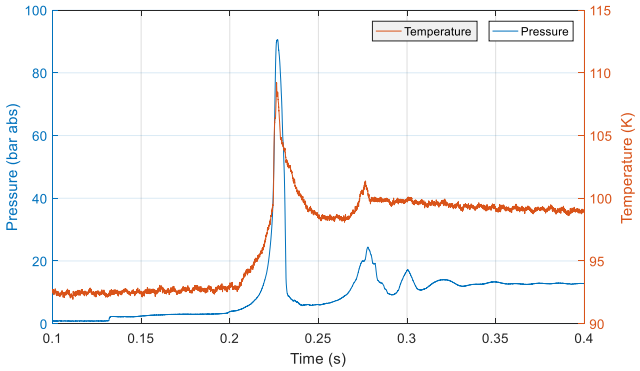

Figure 8. Pressure and temperature evolution at the closed end (P-T module experiments)

The time t=0 in Figure 8 corresponds to the exact moment when the electrical opening signal is sent to the FOV. The evolution of the pressure is not significantly affected by the initial pressure in the line until the liquid front reaches the end of the line. Since the initial line pressure is below the vapor pressure of LN2 for both test conditions, i.e. P-module and P-T module experiments, it might indicate that the vaporization rate of the liquid phase is similar. The ultimate velocity of the liquid front before impact is not affected by the initial pressure conditions in the line since the first pressure pulse reaches the same amplitude. However, the pressure attenuation is slightly higher when the initial pressure in the line is higher as shown in the dimensionless representation of Figure 9.

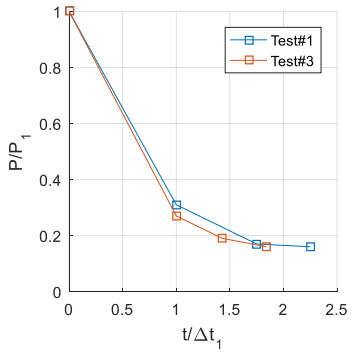

Figure 9. Dimensionless pressure signal attenuation for test #1 (P-module) and test #3 (P-T module)

The temperature of the vapor phase measured at the closed end is constant (around 92K) until the pressure starts to increase at this location. As soon as the pressure increases due the rapid vaporization of the liquid phase, the coaxial thermocouple starts to measure a moderate temperature increase. When the liquid front moves through the line, the vapour phase is getting compressed and its temperature increases of about 6K, from 92 to 98K. Afterwards, when the liquid front arrives at the end of the line, the sudden pressure increase involves an abrupt temperature increase perfectly synchronised with the pressure signal. The maximum temperature (i.e., 109K) is obtained when the pressure level is maximum (i.e., 89bar). With the pressure recovery, the temperature measured by the coaxial thermocouple decreases down to 98.2K. The occurrence of the second pressure peak produces again a temperature increase; however, the magnitude of this peak is much lower. After this point, the fluid temperature is not affected anymore by the occurrence of the following pressure peaks and it decreases gradually with time, stabilizing its value around 97.5K.

The measurement repeatability has been checked with three repetition tests, the data of which are shown in Figure 10. For the time-resolved pressure measured at the closed end, the conclusions are the same as for the P-module experiments. For the time-resolved temperature measurements, the repetition tests show similar evolution. As for the pressure, a time delay is observed between the different tests. The temperature measured in test #5 is slightly higher than in the two other tests due to an higher initial temperature of the instrumented module, i.e., 93.7K compared to 92.5K and 92.3K for test #4 and test #5; respectively. Despite this difference, the repeatability of the time-resolved temperature measurement is considered as satisfactory.

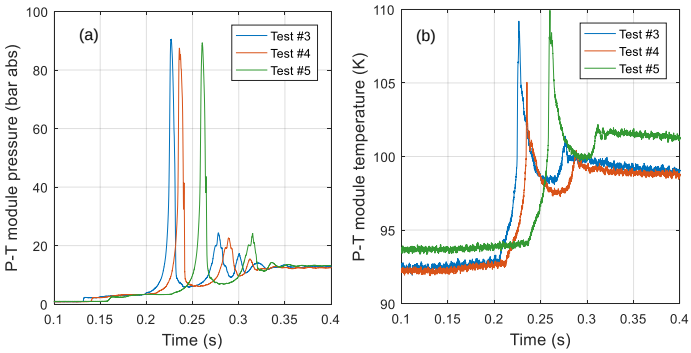

Figure 10. Measurement repeatability for pressure (a) and temperature(b) at the closed end (P-T module)

3. MULTIPHASE FLUID HAMMER SIMULATIONS

1D transient numerical simulations of the multiphase fluid hammer were carried out with the commercial code EcosimPro (v.5.2) using the ESPSS library (v.3.0.3) [11,12]. The code uses the Homogeneous Equilibrium Model (HEM) to model multi-phase flows. For the simulations, 2-phase heat transfer and 2-phase wall friction correlations were used. The model includes the phase change and fluid-structure interaction (FSI). The properties of the fluids are interpolated from the National Institute of Standards and Technology (NIST) thermophysical properties tables. More detailed information about the code can be found in [11,12].

3.1. Numerical model

The experimental data collected with LN2 on the P-module configuration (section 2.4) and on the P-T module configuration (section 2.5) will be used to benchmark the EcosimPro code. Therefore, a numerical model representative of the cryogenic facility has been created with the generic elements of the ESPSS library. It consists in a time-dependent boundary condition representing the pressurized reservoir, three cylindrical pipes connected each other using junction elements to model the 90° bend, a valve to model the variable throat area of the FOV and finally a vertical pipe with a dead end at its extremity to model the test line. A working fluid element is connected to the network to define the working liquid. Constant temperature and pressure have been set in the time-dependent boundary condition. They correspond to the initial values measured experimentally. The working liquid used in the simulation is Real Nitrogen. The opening law defined for the valve is a piecewise-linear approximation of the actual opening law of the FOV shown in Figure 2. Adiabatic conditions are imposed at the external walls of the test line. The initial wall temperature was set to the chilldown temperature measured experimentally. All the simulations have been performed with 200 nodes in the test pipe element according to the node sensitivity analysis performed in [13]. The time-step has been set to 1ms. An aspect that is critical for the fluid hammer simulation is the friction modeling. It has been proved for non-cryogenic liquids that the quasi-steady-state friction factor used by ESPSS underestimates the pressure losses, resulting in higher pressure levels and lower pressure attenuation than in reality [3,4]. The code offers the possibility to correct it by artificially increasing the Darcy friction factor by mean of a multiplier k_f. A k_f -value of 2.5 and 1.9 was recommended by Lema et

al [3,4] for water and ethanol respectively. In the following simulations with liquid nitrogen as working fluid, the friction factor multiplier was set to 2.5.

3.2. Numerical data

Two cases have been simulated with ESPSS to reproduce the different test conditions between the P-module experiments (num. #1) and the P-T module experiments (num. #2) (table 3).

Parameters	Num. #1	Num. #2
Reservoir pressure [bar]	13.25	13.25
Initial line pressure [bar]	0.20	0.85
Reservoir temp. [K]	83	83
Initial line temp. [K]	92	92

Table 3. Test conditions simulated with EcosimPro

3.3. ESPSS simulations of the P-module experiments (num. #1)

Although some limitations have been identified in the numerical code to simulate the fluid hammer [4,5,13], the numerical data is valuable and complementary to experimental data for the understanding of the multiphase fluid hammer phenomena taking place during the priming of evacuated lines. The following description is based on a detailed analysis of the pressure and temperature variables and of the void fraction at each node. The simulation starts as the FOV opens. Since the initial pressure in the line is under the vapor pressure of nitrogen, a rapid vaporization of the liquid flow takes place. A multi-layer structure composed of a vapor layer, a foam layer and a liquid layer is clearly visible in the numerical results during the propagation of the flow along the line (Figure 11a). The vapor initially present in the line and the vapor generated during the vaporization process form the vapor layer at the front. It is followed by the foam layer, which is a two-phase region where vaporization stands [5]. After comes the liquid front. The vapor layer is getting compressed during the process due to the incoming flow and to the continuous vaporization mechanism. As a consequence, the temperature in the vapor layer is increasing due to adiabatic compression as shown in Figure 11b where the temperature evolution calculated at the last node of the line is plotted. After having compressed the vapor layer, the liquid front is compressing the foam layer as well. During the compression of the foam layer, the temperature in the vapor layer stabilizes. That corresponds to the first plateau observed in the temperature evolution (Figure 10b). Finally, the foam and the vapor layers mix together and the liquid front compresses the remaining two-phase layer, inducing a further augmentation of its temperature. The temperature is rapidly decreasing as the liquid phase reaches the closed end of the pipe. The impact of the liquid front is then followed by a small temperature increase due to the compression of the liquid.

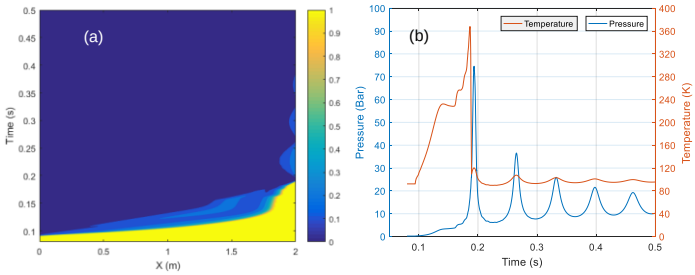

Figure 11. (a) x-t diagram of the void fraction and (b) pressure and temperature evolution at the last node (num. #1)

The numerical simulation reproduces well the generation and the propagation of the compression wave while the flow decelerates. It continues until the whole liquid column stops. At that time, the compression wave reaches the reservoir and is reflected as an expansion wave which travels back. When the expansion wave reaches the end of the pipe, it accelerates the liquid column downwards. The static pressure drops below the saturation pressure and vaporization occurs. A two-phase zone is created at the closed end of the line (Figure 11a). At one point, the movement of the liquid column stops due to pressure at the reservoir side being higher than in the two-phase zone. It reverses the direction of the liquid column and it impacts again to the closed end.

The temporal evolution of the pressure at the last node is compared to the pressure signals measured with the P-module during test #1 and #2 in Figure 12. The simulation anticipates the arrival of the liquid front at the closed end (Figure 12a). However, it is difficult to draw a conclusion on this time delay since the two repetition tests exhibit also a similar delay between them. For an easier comparison, the different signals have been shifted in time to match the occurrence of their first pressure peak (Figure 12b). The pressure increase at the closed end due to the vaporization of the liquid phase entering in the evacuated line is correctly reproduced by the code. The code slightly underestimates the first pressure peak and slightly overestimates the second one. The time interval between these two peaks is well reproduced. The main difference appears on the pressure attenuation in the subsequent peaks. The attenuation is much faster experimentally than numerically. An underestimation of the vaporization rate during the liquid column separation might explain this difference in the pressure attenuation.

With the available experimental data, this point cannot be confirmed, but a larger amount of vapor would amplify the cushion effect on the pressure signal and reduce the speed of sound.

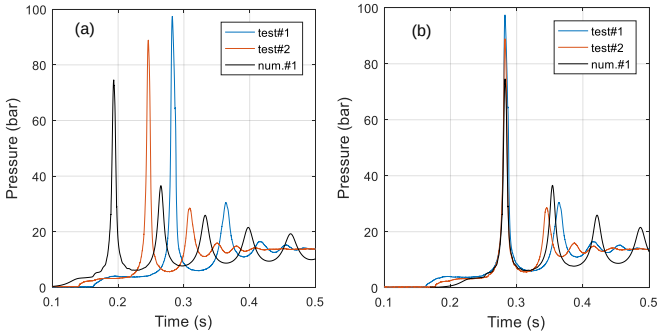

Figure 12. Comparison between simulation #1 and P-module experiments (a. real-time occurrence, b. matching on first peak)

3.4. ESPSS simulations of the P-T module experiments (num. #2)

The second simulation gives a completely different fluid hammer pattern than in the previous simulation. It is worth mentioning that convergence issues have been encountered with these new conditions, i.e. higher initial pressure in the line. The time after which the numerical residuals goes below an acceptable level was sometimes close to the time occurrence of the first pressure peak. Several attempts have been made with different values of friction factor multiplier k_f without any improvement in the convergence. Even at lower k_f value, i.e., k_f =1.5, the calculation stops due to convergence issues. The x-t diagram of the void fraction shows that the liquid front never reaches the end of the line (Figure 13a). A layer of vapor remains at this location and reduces drastically the pressure pulse at impact by cushion effect (Figure 13b). Moreover, the foam layer preceding the liquid front is almost inexistent which tends to indicate that only a very small quantity of vapor is produced. All these observations are questionable for a physical point of view. Indeed, even if the initial pressure in the line is higher than in the previous simulation, i.e., 0.85bar instead of 0.2bar, this pressure is far below the vapor pressure at the considered temperature. Moreover, large discrepancies appear with the experimental data both for pressure and temperature (Figure 14). In this figure, the predicted pressure and temperature evolution have been shifted in time (i.e., 28ms) to match the occurrence of the first pressure peak with the experimental data. The code predicts a first pressure peak 3 times lower than the one measured in the cryogenic facility. This might indicate that the liquid front reaches the closed end in the experiments which was not predicted by the code. Since only a small quantity of vapor is produced in this second simulation, the temperature increase due to the adiabatic compression of the vapor layer while the liquid front progresses, is much lower than in the previous simulation. Furthermore, since the liquid phase does not reach the closed end, the temperature decrease at impact is strongly reduced compared to the previous simulation. We can see in Figure 14b that ESPSS predicts a temperature increase much higher than the one measured in the cryogenic facility. Whereas the fluid temperature reached at the impact location is 350K in both simulations when the liquid front arrives, this temperature measured with the coaxial thermocouple of the P-T module is only 110K. However, it is not possible today with the experimental data available to determine if this difference comes from the modelling hypotheses of the code (e.g. HEM) or from the difficulty to measure time-resolved fluid temperature of such fast phenomenon.

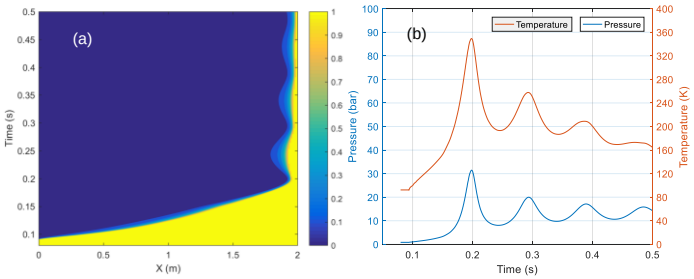

Figure 13. (a) x-t diagram of the void fraction and (b) temporal evolution of the pressure and temperature at the last node (num. #2).

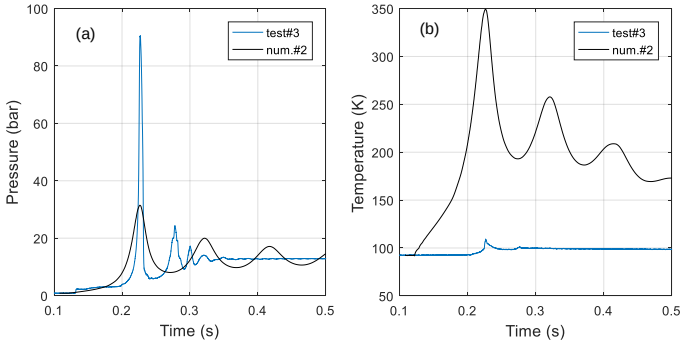

Figure 14. Comparison between the simulation #2 and the P-T module experiments (signals synchronized on the first pressure peak).

4. CONCLUSIONS

A new cryogenic facility has been designed and assembled to allow the detailed characterization of the multiphase fluid hammer phenomenon generated by the discharged of pressurized cryogenic liquid (LN2) into an evacuated line.

Several cryogenic tests have been carried out in this facility. They have demonstrated the technical feasibility of such experimental tests based on multipoint time-resolved pressure and temperature measurements at the closed end of the line (impact location). The measurement repeatability has been verified for each test conditions. The analysis of the generated data has shown that the cryogenic fluid hammer is strongly driven by the high vaporization rate of the liquid phase. It results in a fast pressure attenuation between the successive pressure surges compared to non-cryogenic liquids. The fluid temperature measured at the impact location increases significantly (ΔT~17K) due to the compression of the vapor and foam layers preceding the liquid front. It has been shown experimentally that the initial vacuum level in the line did not change significantly the pattern of the cryogenic fluid hammer since this pressure is always above the saturation pressure.

Numerical simulations of the cryogenic facility at two different initial pressures in the propellant line were carried out with the ESPSS libraries on EcosimPro platform. For the case at low pressure (i.e., evacuated line), the comparison of the numerical results against the experimental data allows the identification with a good confidence level, of the transient multiphase phenomena occurring during the priming. For the case at higher pressure (~1 atm), convergence issues have been encountered. The multiphase flow predicted by the code is questionable from a physical point of view and does not correspond to the experimental observations.

During this study, some trends observed in the fluid temperature measured experimentally at the impact location remain unclear today and needs to be addressed in more details. For a deeper understanding of the cryogenic fluid hammer mechanisms, the measurement layout has been extended to perform high-speed two-phase visualizations at the impact location. The test conditions will be repeated with a new transparent module in place of the instrumentation modules. Comparative tests with water will also been performed with the aim to conclude on the degree level of the physical similarity between cryogenic and non-cryogenic fluid hammer within the same geometrical configuration. The same type of unsteady measurements and flow visualisation will be done for these water tests.

5. ACKNOWLEDGMENTS

This study is supported by the European Space Agency through the TRP activity AO/1-7074/12/NL/RA.

6. REFERENCES

1. Steelant J. (2015), 'Multi-Phase Fluid-Hammer in Aerospace Applications', 12th Int. Conference Pressure Surge, Pressure Surges, Fluid Transients & Water hammer, 18-20/11/2015, Dublin, Ireland
2. Lecourt R. and Steelant J. (2007), `Experimental Investigation of Waterhammer in Simplified Feedlines of Satellite Propulsion System', AIAA Journal of Propulsion and Power, Vol. 23, No. 6, pp 1214-1224, 2007.
3. Lema M. (2013). 'Multi-phase fluid hammer: modeling, experiments and simulations', PhD Thesis Université Libre de Bruxelles and Universidade da Coruna.
4. Lema M., Lopez-Pena F., Rambaud P., Buchlin J.M. and Steelant J. (2015), 'Fluid Hammer with Gas Desorption in a Liquid Filling Pipe System', Experiment in Fluids, 56:180, 2015, DOI 10.1007/s00348-015-2043-2
5. Porca P., Lema M., Steelant J. and Rambaud P. (2014), 'Experimental and Numerical Multiphase-Front Fluid Hammer', J. of Propulsion and Power, March 2014, volume 30, issue 2, pp 368-376, doi: http://arc.aiaa.org/doi/abs/ 10.2514/1.B34832
6. Pinho J., Lema M., Rambaud P. and Steelant J. (2014), 'Multi-Phase Investigation of the Water-hammer Phenomena using the Full Cavitation Model', J. of Propulsion and Power, January 08, 2014, doi: http://arc.aiaa.org /doi/abs/10.2514/1.B34833
7. Bombardieri C., Traudt T. and Manfletti C. (2015), 'Experimental Study of Water Hammer Pressure surge in Spacecraft Feedlines', 6th European Conference for Aerospace Sciences (EUCASS)
8. Yaggy K.L. (1984), 'Analysis of propellant flow into evacuated and pressurized lines', 20th AIAA/SAE/ASME Joint Propulsion Conference
9. Lin T. T., Baker D. (1995), 'Analysis and testing of propellant feed system priming process', Journal of Propulsion and Power 11(3):505-512 1995
10. Anthoine J., Lestrade J.Y., Steelant J., (2014). 'Experimental database with real propellants to study multi-phase fluid hammer phenomena', Space Propulsion 2014, May 2014, Cologne, Germany.

11. Steelant J., De Rosa M., Moral J. and Pérez R. (2010), 'ESPSS Simulation Platform', Space Propulsion 2010, San Sebastian, Spain, 3-6 May 2010.
12. Di Matteo F. and Steelant J. (2013), 'Multi-Disciplinary Propulsion Simulations at Engineering Level by means of the European Space Propulsion System Simulation ESPSS', RTO / AVT/VKI Lecture Series on Fluid Dynamics Associated to Launcher Developers, EN-AVT-206-06, Von Karman Institute, St. Genesius-Rode, Belgium, 15-17/04/2013.
13. Gouriet J-B., Buchlin J-M., Lema M., Petro Z., Vetrano R., Peveroni L. and Steelant J. (2015), 'Multiphase fluid hammer with non-cryogenic and cryogenic fluids', 8th European Symposium on Aerothermodynamics for Space Vehicles, March 2015, Lisbon, Portuga